



Effect of Particle and Substrate Pre-heating on the Oxide Layer and Material Jet Formation in Solid-State Spray Deposition: A Numerical Study

P. Khamsepour¹ · C. Moreau¹ · A. Dolatabadi²

Submitted: 8 August 2022 / in revised form: 11 November 2022 / Accepted: 15 November 2022 / Published online: 9 December 2022
© ASM International 2022

Abstract In a solid-state deposition technique such as cold spray (CS) or high-velocity air-fuel (HVOF), particle and substrate initial conditions play a crucial role in particle deformation and its adhesion strength to the substrate. In these thermal spray techniques, the deposited particle and the substrate are required to deform plastically; hence, both components are usually metallic. An oxide layer at the surface of these metallic components may avoid producing a metallurgical bonding and strong adhesion between them. To better understand the effect of particle and substrate initial conditions, e.g., particle velocity, particle temperature, and substrate temperature, on the formation of metallurgical bonding, it is necessary to examine particle and substrate oxide layer failure. In this work, the effect of a 20 μm Ti-6Al-4V particle and a Ti-6Al-4V substrate initial conditions on the failure of their oxide layer during impact has been studied. The results show that the presence of an oxide layer increases the required critical velocity for particle adhesion on the substrate. Furthermore, regardless of the chosen initial conditions, the particle oxide layer would fail in the adiabatic shear instability region because of the severe deformation that the particle experiences upon impact. This study shows that a stronger bonding between the deposited particle and the substrate can be

achieved by increasing the particle velocity and substrate temperature, as they increase the extent of the failed oxide layer region of the substrate. Rising particle temperature increases particle deformation and has no significant effect on the adhesion between the particle and substrate.

Keywords adiabatic shear instability region · cold spray · elastic-plastic simulation · high velocity air-fuel · material jet production · metallurgical bonding · oxide layer failure

Introduction

Cold spray is a unique thermal spray technique that allows solid-state deposition without oxidation or decomposition (Ref 1, 2). In this process, solid particles impact the substrate surface at a high velocity while retaining their low temperature. Upon impact, particles severely deform at a very high strain rate (up to 10^9 s^{-1}), leading to the oxide layer failure, followed by a metallurgical bonding, and eventually the formation of coatings (Ref 3-5). In fact, the brittle oxide layer will not undergo the same significant amount of deformation that a particle or a substrate goes through which results in its failure (Ref 6). The failure of the oxide layer produces small oxide debris and provides two new metallic surfaces in direct contact (Ref 7).

The produced oxide debris must be ejected with the help of adiabatic shear instability (ASI) and the material jetting (Ref 8, 9). ASI is a transformed local shear strain caused by the pressure gradient created during the particle deformation. ASI helps thermal softening, governs the deformation and significantly increases the particle temperature. The higher temperature and thermal softening combination create an out-flowing material jet that ejects the broken oxide layer (Ref 10). Hassani-Gangaraj et al. (Ref 11)

✉ P. Khamsepour
peymankhamsepour@gmail.com

A. Dolatabadi
dolat@mie.utoronto.ca

¹ Department of Mechanical, Industrial and Aerospace Engineering, Concordia University, Montreal, Québec, Canada

² Department of Mechanical and Industrial Engineering, University of Toronto, Toronto, ON, Canada

suggested that the thermal softening is not the cause of material jet formation. They state that the produced tensile stress at the edges of the contact area of the deposited particle and substrate is the reason for material jet formation. Chen et al. (Ref 12) also studied the de-bonded sprayed solid particles and showed that a metallurgical bonding could be formed only after the oxide layer fails and the newly formed metallic surfaces are put in direct contact.

The effects of particle velocity on the adhesive strength of cold spray deposited particles have been investigated previously (Ref 13–18). As an example, Legoux et al. used a low-pressure cold spray system to show that increasing particle velocity could enhance adhesive strength and deposition efficiency (Ref 14). However, it is not possible to increase particle velocity limitless (Ref 15). For increasing the adhesive strength even more, it has been proposed that increasing substrate temperature can play a key role (Ref 13–18). A study by Xie et al. suggests that substrate pre-heating can cause softening, crater depth enhancement and more substrate deformation. As a result, a material jet can be produced from the deposited particle and the substrate leading to bonding with higher adhesive strength (Ref 16). However, it is worth noting that increasing the substrate temperature can increase the substrate oxide layer thickness and alter the required critical velocity for bonding (Ref 13).

Considering current capabilities, the study of particle deformation and oxide layer failure using experimental techniques is very difficult because these phenomena occur in tens of nanoseconds (Ref 19). This necessitates the use of a modeling system as an alternative approach. The finite element method (FEM) has been widely used for studying the deformation of deposited particles using CS on the assumption that a particle is in an Eulerian or Lagrangian framework (Ref 20–22). In the previous studies, FEM was also utilized to assess the effect of the velocity and temperature of a particle on its deformation upon impact (Ref 22, 23). The behavior of the oxide layer of a particle when impacting the substrate during the CS process has been widely studied (Ref 6, 24, 25). Rahmati et al. (Ref 6) assumed that the oxide layer could deform until it reaches failure displacement which has a low numerical value because of its brittleness. They showed that the particle core dominates the deformation process. This means that the material response of the oxide layer is insignificant due to the high kinetic energy of the impact. Hence, that oxide layer would deform independent from its material properties, and its failure would only depend on displacement at the failure. They also investigated the effect of the failure displacement of the oxide layer of copper on its failure, by developing a model to illustrate the bonded and de-bonded areas of the impacted particle (Ref 6).

This study tries to continue the work that has been carried out before by Rahmati et al. (Ref 6) by taking the effect of particle and substrate temperature on oxide layer failure into consideration. Since a nanometric-scale oxide layer has been proven to show ductile behavior, both using experiment and molecular dynamic methods (Ref 6, 26), an elastic-plastic damage numerical examination has been developed by assuming that a 20 μm Ti-6Al-4V particle is deposited using HVOF toward a Ti-6Al-4V substrate, while both parts are covered with an 80-nm oxide layer.

Numerical Methodology

Mie–Grüneisen Equation of State

The Mie–Grüneisen equation of state (EoS) was used to investigate the elastic deformation of deposited particles. This model is based on crystal structure and a connection among internal energy, thermal vibrational energy, and potential energy at zero temperature (Ref 5–8). The initial form of the Mie–Grüneisen EoS is obtained using the vibrational theorem and the Grüneisen equation, presented as Eq 1, (Ref 27, 28):

$$P - P_H = \Gamma_0 \frac{p_0}{p} (E_m - E_H) \quad (\text{Eq 1})$$

where P is the total pressure, E_m denotes the internal energy per unit mass, P_H stands for the Hugoniot pressure, and E_H indicates the specific energy. Moreover, Γ_0 is the material constant, p_0 is the reference density, and p represents the pressure stress. The values of Hugoniot energy and Hugoniot pressure can, respectively, be calculated via Eq 2 and 3 (Ref 27, 28):

$$E_H = \frac{P_H \eta}{2p_0} \quad (\text{Eq 2})$$

$$P_H = \frac{p_0 c_0^2 \eta}{(1 - s\eta)^2} \quad (\text{Eq 3})$$

where η (nominal compressive volumetric strain) is equal to $1 - p_0/p$ and $p_0 c_0^2$ designates the elastic modulus at a low nominal strain rate. Furthermore, c_0 and s are the material constants that can make a link between shock velocity (U_s) and particle velocity (U_p). The final form of the Mie–Grüneisen EoS is obtained using Eq 4 (Ref 27, 28):

$$P = \frac{p_0 c_0^2 \eta}{(1 - s\eta)^2} \left(1 - \frac{\Gamma_0 \eta}{2} \right) + \Gamma_0 p_0 E_m \quad (\text{Eq 4})$$

As this model can only represent the hydrostatic behavior, elastic models and shear modulus were used to examine the deviatoric behavior (Ref 5).

Johnson–Cook Model

A Johnson–Cook plasticity model was used to investigate deformation at a high strain rate. This model is reproduced in Eq 5 below (Ref 5):

$$\sigma = \left(A + B\dot{\epsilon}_p^n \right) \left(1 + C \ln \frac{\dot{\epsilon}_p}{\dot{\epsilon}_0} \right) \left(1 - \left(\frac{T - T_r}{T_m - T_r} \right)^m \right) \tag{Eq 5}$$

where A , B , C , n , and m are the material constants, ϵ_p , $\dot{\epsilon}_p$, σ , $\dot{\epsilon}_0$, T_r , T_m , and T are the equivalent plastic strain, plastic strain rate, flow stress, reference strain rate, reference temperature, melting point, and temperature, respectively.

Johnson–Cook Damage Model

A damage model assumes that a damage or a crack is initiated when the ratio of equivalent plastic to the equivalent fracture strain of $(\Delta\bar{\epsilon})$ to equivalent fracture strain $(\bar{\epsilon}_f)$ equals 1, as shown in Eq 6 (Ref 28-31):

$$D = \sum \frac{\Delta\bar{\epsilon}}{\bar{\epsilon}_f} = 1 \tag{Eq 6}$$

The present study used the Johnson–Cook damage model in connection with the Johnson–Cook plasticity model to examine fracture initiation. To calculate the equivalent fracture strain $(\bar{\epsilon}_f)$, Eq 7 was used (Ref 28-31):

$$\bar{\epsilon}_f = \left[d_1 + d_2 \cdot \exp(d_3 \eta) \right] \times \left[1 + d_4 \cdot \ln \left(\frac{\dot{\epsilon}}{\dot{\epsilon}_0} \right) \right] \times \left[1 + d_5 \cdot \left(\frac{T - T_{room}}{T_m - T_{room}} \right) \right] \tag{Eq 7}$$

where d_1 , d_2 , d_3 , d_4 , and d_5 represent the initial failure strain, exponential factor, triaxiality factor, strain rate factor, and temperature factor, respectively. It is necessary to consider damage evolution to examine the oxide layer’s failure pattern during the deformation of the deposited particles (Ref 28-31). Since it is well established in the literature, both experimentally and numerically that the thin brittle oxide layer presents some important and non-negligible ductility (Ref 6, 26, 32-39), a ductile fracture model like Johnson–Cook has been selected to analyze the failure of the thin brittle layer (Ref 6, 40).

Damage Evolution Law

The reduction rate of material stiffness can be defined using the damage evolution law. In the current study, this rate was determined on the basis of effective plastic displacement (\bar{u}^{pl}) and through the use of evolution equations, Eq 8 and 9 (Ref 6, 28).

$$\dot{\bar{u}}^{pl} = L \dot{\bar{\epsilon}}^{pl} \tag{Eq 8}$$

$$\dot{d} = \frac{L \dot{\bar{\epsilon}}^{pl}}{\bar{u}_f^{pl}} = \frac{\dot{\bar{u}}^{pl}}{\bar{u}_f^{pl}} \tag{Eq 9}$$

where L is the element length, \bar{u}^{pl} indicates the effective plastic displacement, $\dot{\bar{\epsilon}}^{pl}$ denotes the equivalent plastic strain rate, \bar{u}_f^{pl} is the effective plastic displacement at the failure point, and \dot{d} stands for the damage variable rate.

A linear type of damage evolution was used, where material stiffness is assumed to be fully reduced ($d = 1$) when effective plastic displacement reaches the fracture value $(\bar{u}^{pl} = \bar{u}_f^{pl})$, as shown in Fig. 1. In the damage evolution law for examining brittle fracture, the value of \bar{u}_f^{pl} was set to zero. However, for ductile fracture, the \bar{u}_f^{pl} value depends on mesh size, and its accurate value must be obtained using the experimental examination. Here, in this research, the same range tested in the literature (Ref 6, 28) was used to investigate the failure of the oxide layer since carrying out the experimental work was beyond the scope of this study.

Finite Element Method

The deformation of a Ti-6Al-4V solid-state particle deposited using either HVOF or CS was studied, drawing upon the Lagrangian technique on the FEM software ABAQUS/Explicit (Ref 6). All simulations have been carried on for 8 ns which is because the oxide layers fail at the first nanoseconds of the impact. After oxide layer breakage, the particle and substrate deformation cause the production of material jet. Hence, the selected duration for examining the oxide layer failure would not only provide a fair comparison of the oxide layer failure but also avoids having highly distorted elements. Scanning electron microscopy (SEM) micrograph and particle size distribution curve of Ti-6Al-4V powder are shown in Fig. 2. Ti-6Al-4V powder consists of spherical particles with particle diameters centered along a single mode, with maximal volume frequency at 22 μm. The D10, D50, and D90 values are 14, 20, and 29 μm, respectively, showing that the particle size distribution of Ti-6Al-4V powder is very narrow (Fig. 2b). Thus, for this simulation, it was assumed that the 20 μm Ti-6Al-4V particle impacts a Ti-6Al-4V substrate. Figure 3 demonstrates the initial conditions of Ti-6Al-4V particle and substrate used to investigate oxide layer failure during the deposition process. An 80-nm thin brittle layer which can act as the similar to the brittle titanium oxide layer was assumed at the surface of the substrate and particle to examine oxide layer failure during the particle impact (Fig. 3). This thickness falls in the

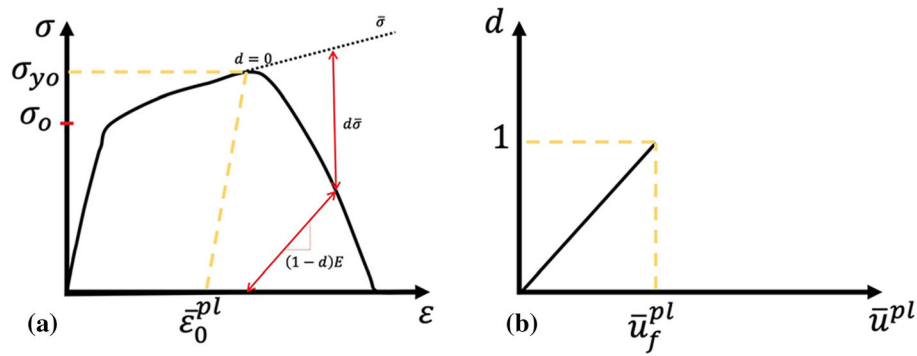


Fig. 1 (a) Schematic stress–strain diagram of material with progressive damage reduction and (b) linear damage evolution in terms of plastic displacement. Adapted by permission from Springer Nature Customer Service Centre GmbH: Springer Nature, Journal of Thermal

Spray Technology, A Numerical Approach to Study the Oxide Layer Effect on Adhesion in Cold Spray, Saeed Rahmati et al., Copyright 2021 (Ref 6)

Fig. 2 (a) SEM micrographs and (b) size distribution of the Ti-6Al-4V powder

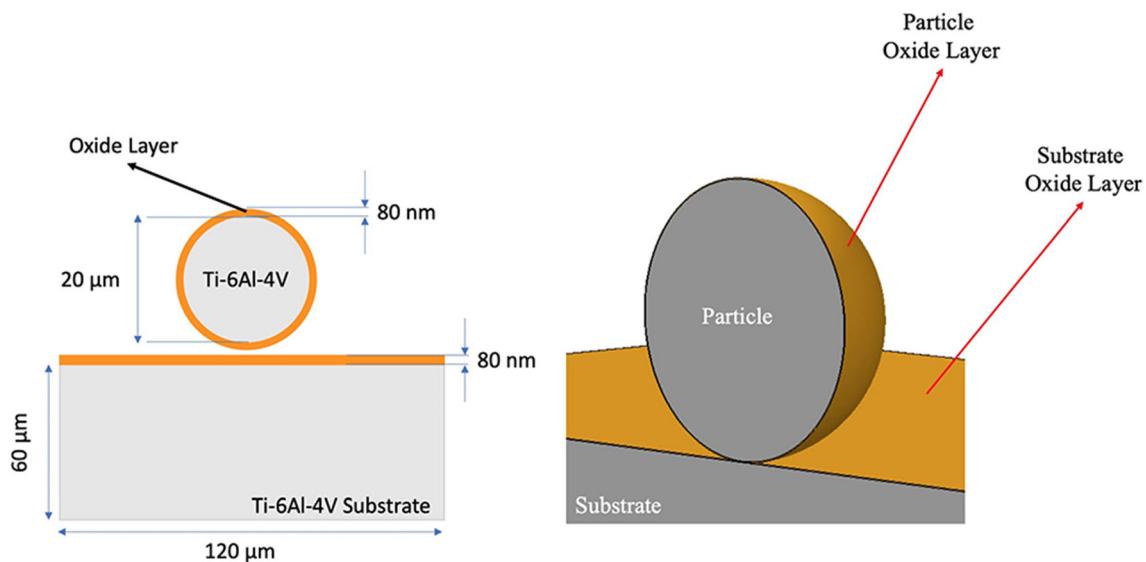
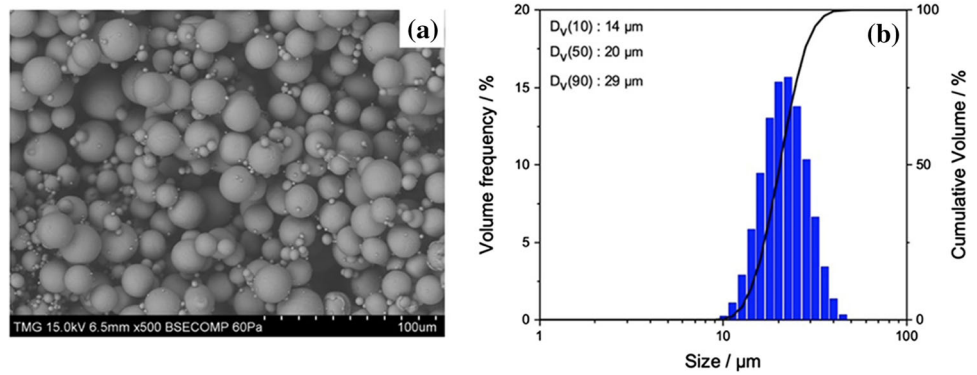


Fig. 3 The geometry was used to investigate the oxide layer failure during the impact of a Ti-6Al-4V particle

range used in the previous studies (Ref 6, 24, 25, 32, 41). Additionally, during depositing solid particles using HVAF, due to the high temperature of the existing flame, oxidation happens which can increase the oxide layer

thickness significantly. A 3D geometry is also given in Fig. 3. It is worth noting that the particle diameter with oxide is exactly 20.16 μm ; however, to simplify the reading of the text, it would namely be called a 20- μm Ti-6Al-

4V particle. All the material constants used for this simulation are laid out in Table 1 (Ref 32, 41-44). The same material constant used for the core particle was used for the oxide layers. This is because the particle kinetic energy is significantly high which deforms the oxide films independently from their own properties. Hence, the only parameter that is important is the brittleness of the oxide film which is defined by using \bar{u}_f^{pl} (Ref 6). It must be noted that changes in density, shear modulus, heat conductivity, and heat capacity with temperature were considered using the formulations noted in the literature (Ref 43). Also, according to the literature (Ref 45, 46), when a Ti-6Al-4V sample is subjected to an elevated temperature environment, titanium oxide can be formed. Hence, in this study, it is assumed that titanium oxide covered both deposited particles and the substrate surface.

All simulations were performed in the Lagrangian framework. After the application of material constants, the dynamic explicit solver was used. Once the parts were assembled, the interaction was defined using a friction coefficient of 0.3 and the “penalty” option. The exchange between the surfaces was assumed “general” (Ref 6, 8, 23). To define the tie between the deposited particle and its oxide layer, the “surface to surface” option was the most efficient one. After applying initial velocity and temperature to the particle and the substrate, each part was

meshed. The mesh size for the particle, the substrate area under the impact, and the oxide layer were assumed to be 0.5 μm , which is 1/40 of particle diameter and falls in an acceptable range based on the mesh size presented in the literature (Ref 6, 19). It is worth noting that one and six elements have been selected on particle and substrate oxide layers thickness, respectively. The mesh type for all the parts was defined as C3D8RT (an 8-node thermally coupled brick, trilinear displacement, temperature, reduced integration, and hourglass control) with mesh distortion control to increase the accuracy of the results (Ref 6, 19).

The present study assumed that the Ti-6Al-4V particle deposited using CS (particle and substrate temperature was 298 K) impacted the Ti-6Al-4V substrate once without considering oxide layers and the other time both parts are covered with an 80-nm oxide layer. The effective plastic displacement of the oxide layer at the failure point (\bar{u}_f^{pl}) was assumed 0.00025 (Ref 6). Such numerical investigations were conducted to examine the effect of the oxide layer on the final deformed shape of the deposited particle. Also, during depositing solid particles using HVAF, deposited particles and substrate initial conditions play a key role in the failure of the oxide layer and bonding strength. Hence, to study the role of particle velocity, particle temperature, and substrate temperature on particle and substrate oxide layer failure, the selected initial conditions shown in Table 2 were used. It is worth noting that particle velocity effect on particle oxide layer failure was examined in previous literature (Ref 6). However, since the substrate oxide layer was not taken into account, this paper investigates particle velocity to gain more understanding on its effect on the failure of both particle and substrate oxide layer.

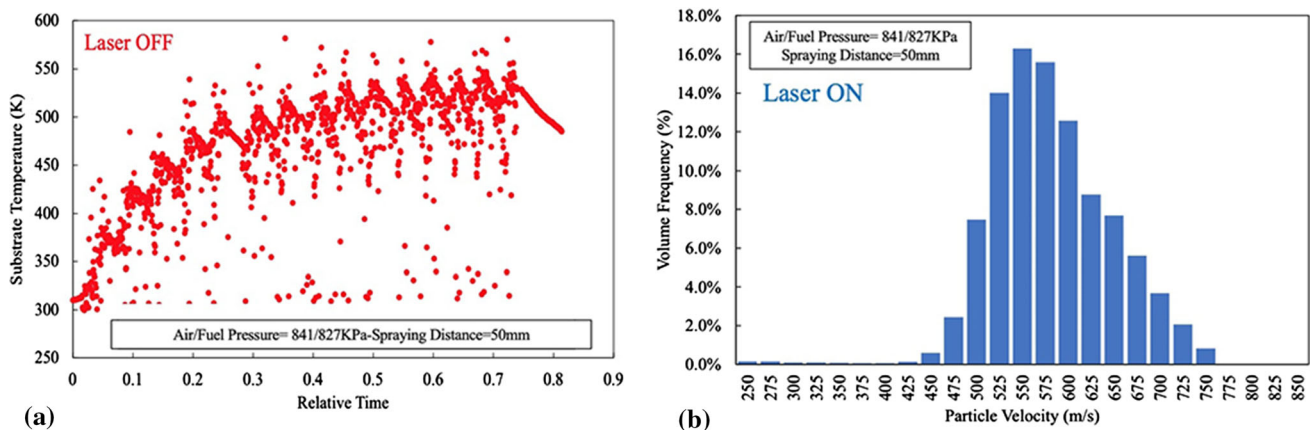
All noted initial conditions noted in Table 2 are obtained using experimental data acquired during deposition of Ti-6Al-4V particles using an internal-diameter HVAF (ID-HVAF) system (Uniquecoat Technologies LLC, Oilville, USA). ID-HVAF has three different convergent-divergent nozzles in which their difference is their length. The spraying distance for depositing coatings is in the range of 50 to 75 mm. During the experimental examination of the potential of ID-HVAF for producing Ti-6Al-4V coatings, substrate temperatures were selected from the experimental observation using an infrared camera (Teledyne FLIR, A320), while Ti-6Al-4V particles were impinging on already deposited Ti-6Al-4V particles, as shown in Fig. 4(a). The in-flight particles velocity and temperature were measured by the DPV-evolution (company, model) using light signal radiated from the heated particles above 1273 K. However, when DPV was worked in hot particle mode with an inactive laser, only the small burning particles were detected. Therefore, the cold particle mode of

Table 1 Ti-6Al-4V material constants were used in the simulation (Ref 42-44)

Property	Ti6Al4V
Density (kg/m^3)	4430
Shear modulus (GPa)	41.9
$C_0(\frac{m}{s})$	5130
s_0	1.03
Γ_0	1.23
A (MPa)	8.62
B (MPa)	331
C	0.012
m	1.1
n	0.34
$T_m(K)$	1903
$T_r(K)$	298
Conductivity ($W/m.K$)	6.6
Heat Capacity ($J/Kg.K$)	536
d_1	- 0.09
d_2	0.25
d_3	- 0.5
d_4	0.014
d_5	3.87

Table 2 Particle and substrate initial conditions were used to study the oxide layer failure

Studied initial condition	Particle velocity, m/s	Particle temperature, K	Substrate temperature, K
Particle velocity effect	550	1073	298
	750	1073	298
	950	1073	298
Particle temperature effect	750	873	298
	750	1073	298
	750	1273	298
Substrate temperature effect	750	1073	298
	750	1073	373
	750	1073	473

**Fig. 4** The variation in (a) substrate temperature monitored using an IR camera and (b) the distribution of in-flight particle velocity detected using cold mode of DPV using an active laser during the deposition of a Ti-6Al-4V coating using an inner-diameter HVOF gun

DPV with an active laser was used to monitor the velocity of larger and cooler in-flight particles. Figure 4(b) shows the distribution of the obtained particle velocity using the spraying condition in which air/fuel pressure is 841/827 KPa and the spraying distance is 50 mm. It is worth noting that a difference of 14 KPa between air and fuel pressure is necessary to obtain a stable flame for the deposition. The range of in-flight particle velocity was between 450 and 1050 m/s. Therefore, the selected initial particle velocity noted in Table 2 falls into the in-flight particles velocity measured by DPV. However, it was not possible to produce coating by depositing the particles shown in Fig. 2 due to the low in-flight particle velocity. Hence, in this study, a higher particle velocity (950 m/s) compared to DPV measurement was also selected as one of the initial conditions. As mentioned above, DPV is not able to measure particle temperature below 1273 K; hence, 873, 1073, and 1273 K were selected as particle temperature (Ref 47, 48). However, computational fluid dynamic (CFD) models can be used to accurately estimate in-flight particles temperature which was beyond the scope of this paper. In the end, it is worth noting that the detected in-flight particle size was

compared to the initial particle size (Fig. 2b) in order to calibrate the DPV cold mode.

Results and Discussion

Effect of Oxide Layer on Particle Deformation

Figure 5 shows the final deformed shape of the particle at 30 ns after the impact for the cases with and without oxide layers. For comparison purposes, the SEM micrograph of an around 20 μm Ti-6Al-4V particle deposited on a Ti-6Al-4V substrate using a cold spray (298 K) at an average velocity of 782 ± 152 m/s is also shown in Fig. 5(d) (Ref 50). Two different simulations were carried out to explore the effect of the oxide layer on the final shape of the particle. First, an 80-nm oxide layer was assumed to be around the 20 μm Ti-6Al-4V particle and at the surface of the substrate. Then, it was assumed that the particle impacted without any oxide layer. In both cases, particle temperature and substrate temperature were 298 K, and particle velocity was once 750 m/s for the time no oxide layer has been

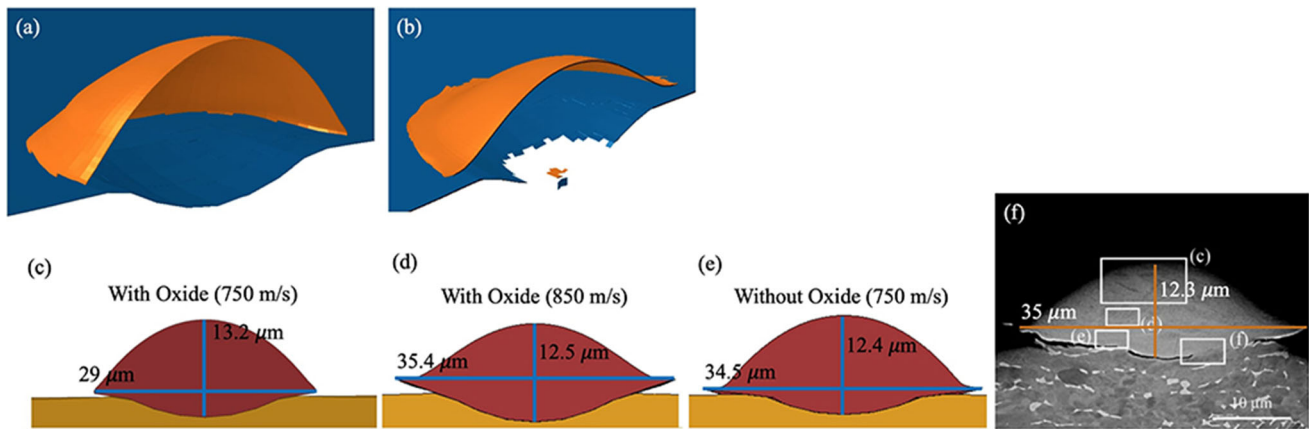


Fig. 5 (a) Oxide layer when impact velocity is 750 m/s, (b) oxide layer when impact velocity is 850 m/s, (c) the final deformed shape of the particle with oxide layers impacted at 750 m/s, (d) the final deformed shape of the particle with oxide layers impacted at 850 m/s, (e) the final deformed shape of the particle without oxide layers impacted at 750 m/s, and (f) the experimental result of a 20 μm Ti-

6Al-4V particle deposited on a Ti-6Al-4V substrate using the cold spray at a velocity of 782 ± 152 m/s. Reprinted from Materials Letters, Vol. 244, Venkata Naga Vamsi Munagala et al. The influence of powder properties on the adhesion strength and microstructural evolution of cold sprayed Ti6Al4V single splats, pg. 58–61, Copyright 2019, with permission from Elsevier (Ref 50)

considered and 750 and 850 m/s for the time that particle and substrate were covered with an 80-nm oxide layer. Effective plastic displacement at the failure point for both oxide layers was assumed 0.00025. In Fig. 5(a) and (b), the dark blue color represents the substrate oxide layer, while the orange color represents the particle oxide layer. Also, the white area in all the oxide layer examinations illustrates the region in which the oxide layer is only broken. As depicted in Fig. 5, the particle in all three conditions deformed significantly. Figure 5a shows that when particle velocity is 750 m/s, substrate oxide did not fail meaning that no bonding can be formed. Additionally, Fig. 5(c) shows that the deformed particle does not have the same dimension compared to the reported experimental results (Fig. 5f). Hence, to enhance the deformation and to fail substrate oxide layer, it is necessary to increase impact velocity from 750 m/s to 850 m/s. Figure 5(b) shows that when impact velocity is 850 m/s, some parts of oxide layers present a curvature-like shape illustrating that the oxide layer deformed plastically before its failure due to the particle's high level of kinetic energy similar to the results presented in the literature (Ref 6). By comparing the simulated and the experimental results (Ref 50), it was found that regardless of the presence of the oxide layer, the numerical method can predict accurately the shape of the deformed Ti-6Al-4V particle. However, in the numerical study, to accurately predict the deformed particle size when both particle and substrate are covered with an oxide layer, the impact velocity should be increased by 100 m/s, Fig. 5(b) to (d). This means that having an oxide layer around the particle and/or substrate would increase the required velocity in which the particle can adhere to

substrate metallurgically. This finding is aligned with previous literature suggesting that the presence of oxide layer affects the required critical velocity (Ref 49, 50).

Effect of Oxide Layer on Material Jet Formation

In the next step, in order to analyze the material jet formation, it is assumed that by using HVAF, an elevated temperature solid particle impacts a substrate, both covered with an oxide layer. In order to do so, particle temperature and velocity are assumed to be 1073 K and 950 m/s, respectively, while the substrate temperature is kept at 298 K. The effective plastic displacement for the oxide layer was 0.0005. Figure 6 compares the pressure stress distribution in particle and substrate as a function of time after the impact. A pressure gradient is distributed in both particle and substrate when the particle impacted the substrate. Over time, this pressure gradient increased in a ring-shaped region known as the ASI region (Ref 10, 11). As shown in Fig. 6, pressure stress was higher in the ring-shaped ASI region, in both particle and substrate. The simulation results in Fig. 6 demonstrate that at the beginning of the impact, the pressure stress is distributed at the contact area but with the passage of time tensile stress is formed at the tip of the contact area (red circles). This tensile stress becomes more significant with time leading to the ejection of the materials. In the end, it is worth noting that the gray and black colors seen in Fig. 6 are regions with the stresses higher or lower than the used range in the color bar. The plastic strain (PE) distribution, as shown in Fig. 7, indicates that an increase in the pressure stress causes more deformation in the ASI region. Figure 8 shows

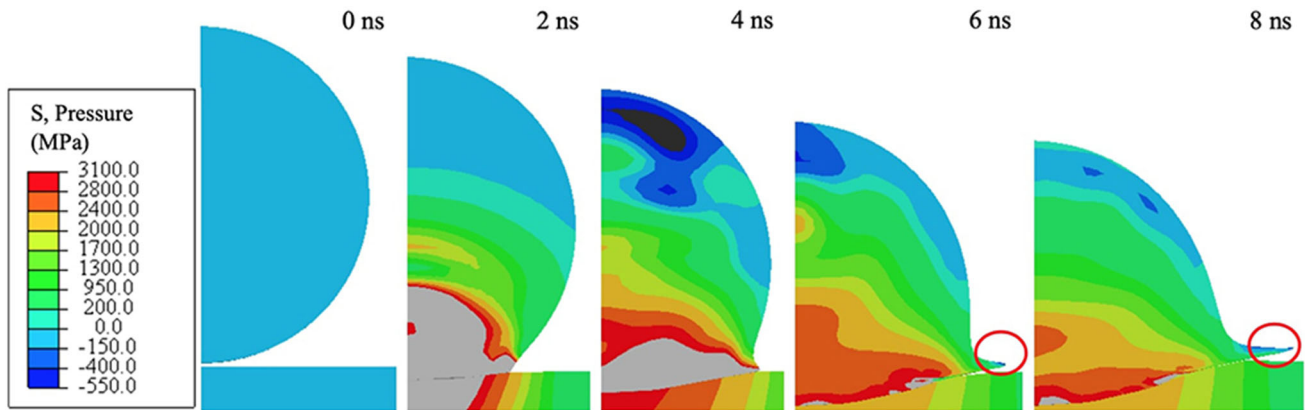


Fig. 6 The examination of the pressure stress distribution in both particle and substrate as a function of time while Ti-6Al-4V particle temperature is 1073 K and its velocity is 950 m/s, and the substrate temperature is 298 K

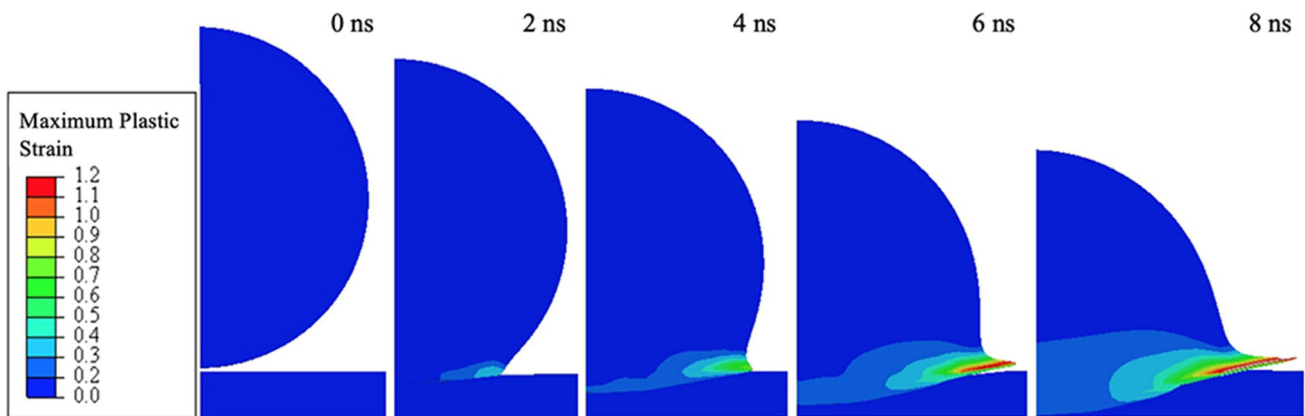


Fig. 7 The examination of the plastic strain distribution in both particle and substrate by the passage of time while Ti-6Al-4V particle temperature is 1073 K and its velocity is 950 m/s, and the substrate temperature is 298 K

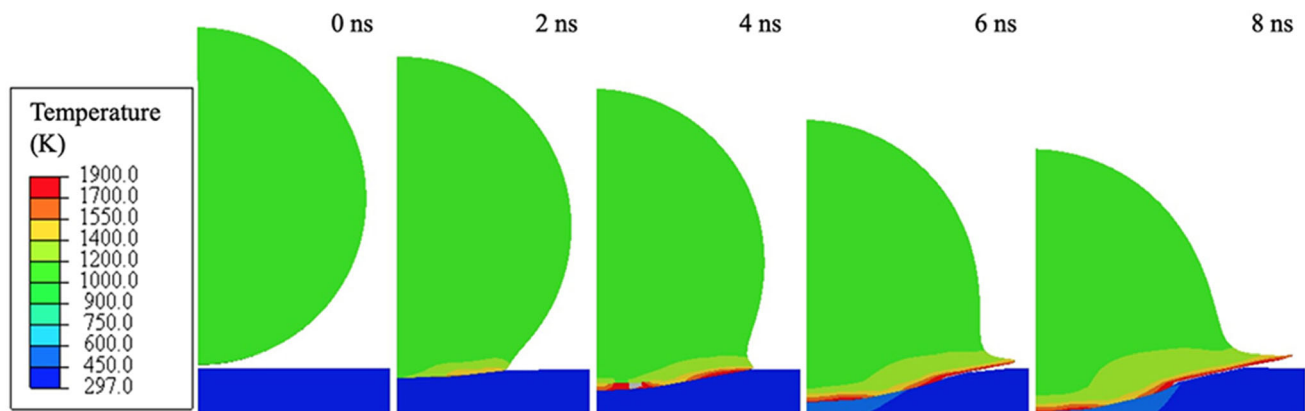
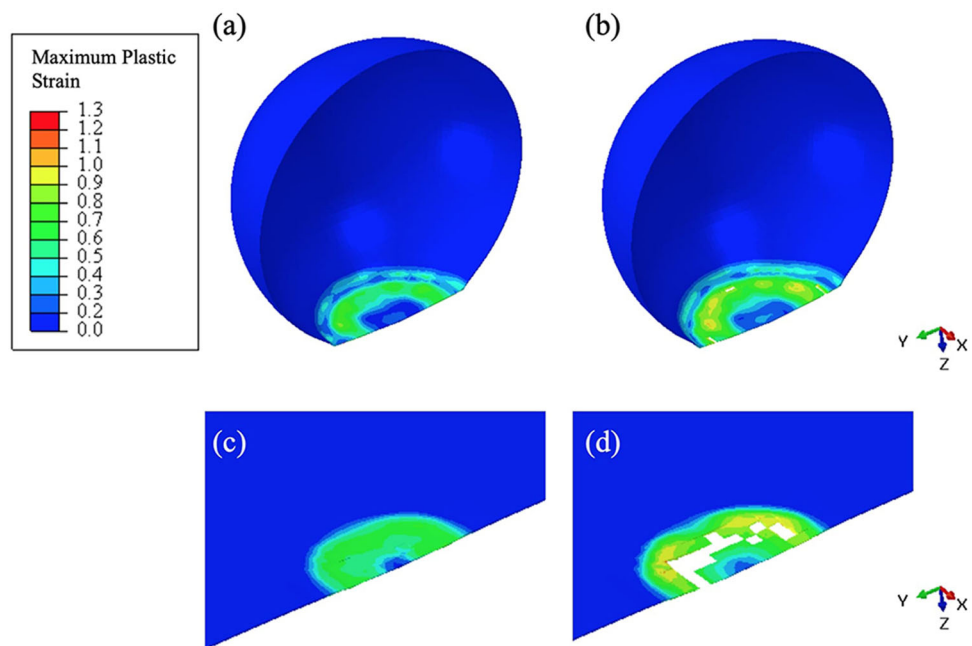


Fig. 8 The examination of the temperature distribution in both particle and substrate by the passage of time while Ti-6Al-4V particle temperature is 1073 K and its velocity is 950 m/s, and the substrate temperature is 298 K

the temperature distribution at the interface of the particle and substrate. In the ASI region, due to the high amount of deformation, the temperature raised significantly which caused thermal softening. Also, the produced tensile stress at the edge of the impact surface has ejected the softened

material of the particle and substrate and produced a material jet, as illustrated in Fig. 6. Therefore, the same reported behavior that causes the formation of a material jet in cold spray (Ref 10-12) can be observed for deposited solid particle covered with oxide layer using HVAF.

Fig. 9 The investigation of the plastic strain of (a) particle oxide layer at 1.4 ns, (b) particle oxide layer at 1.6 ns, (c) substrate oxide layer at 0.8 ns, and (d) substrate oxide layer at 1 ns, before and after the oxide layer fracture occurs



In addition, as illustrated in Fig. 9, the oxide layer failure occurs on the path of the ASI region where the plastic strain is higher due to larger deformation. The fractured pieces of the oxide layer are ejected with the help of the material jet before the formation of metallurgical bonding. Figure 9(a) shows that at 1.4 ns, the oxide layer went through a plastic deformation before it started to fail. At 1.6 ns (Fig. 9b), the oxide layer went through a higher degree of deformation and failed in the regions where the plastic strain was higher. At the same time, the oxide layer on the substrate surface failed with a similar mechanism, as illustrated in Fig. 9(c-d), which means that when the plastic strain in a ring-shaped ASI region increases, the oxide layer fails.

Parameters Influencing the Oxide Layer Failure

Particle Velocity

To analyze the effect of particle velocity on oxide layer failure and the adhesion of the particle and substrate, it was assumed that a 20- μm Ti-6Al-4V particle was deposited using HVAF at the temperature of 1073 K and various velocities between 550 and 950 m/s, while substrate temperature stayed constant at 298 K. Increasing particle velocity provides more kinetic energy required for particle deformation; hence, the particle can go through more deformation. Figure 10 shows the equivalent plastic strain changes by the passage of time of the deposited particle and substrate. As shown in Fig. 10(a), an increase in particle velocity raises the equivalent plastic strain value showing an increase in particle deformation. Additionally,

increasing the particle velocity enhanced substrate equivalent plastic strain and substrate deformation (Fig. 10b). The increase in the deformation of the deposited particle and substrate accelerates oxide layer failure.

Figure 11 shows the effect of impact velocity on the oxide layer failure, while the particle temperature is 1073 K and the substrate temperature is 298 K. The simulation results shown in Fig. 11 indicate that as the particle velocity rises, the particle flattening ratio and deformation increase. Also, a higher particle velocity causes more deformation of the substrate surface and increases the particle penetration into the substrate. For the particle, as the velocity increases from 550 to 950 m/s, the particle goes through more degrees of deformation, and its oxide layer quickly fails. To produce a region with the possibility of making a metallurgical bonding, the oxide layer of the substrate needs to be eliminated as well. This only can be achieved when particle velocity is 950 m/s, as shown in Fig. 11(c). These results confirm the significant impact of particle velocity on the formation of metallurgical bonding. The noted findings can be validated by previous studies (Ref 51, 52). As such, Huang et al. (Ref 51) studied the effect of the particle velocity on the tensile strength of the coatings manufactured by cold spray. They concluded that increasing particle velocity could enhance particle and substrate deformation, increasing the coating's adhesive strength and tensile strength. Additionally, an interesting experimental examination showed that a higher particle velocity can increase the possibility of oxide layer delamination. However, at the south pole of the impacted particle, an island of oxide layer would be oxide due to the low degree of deformation (Ref 52).

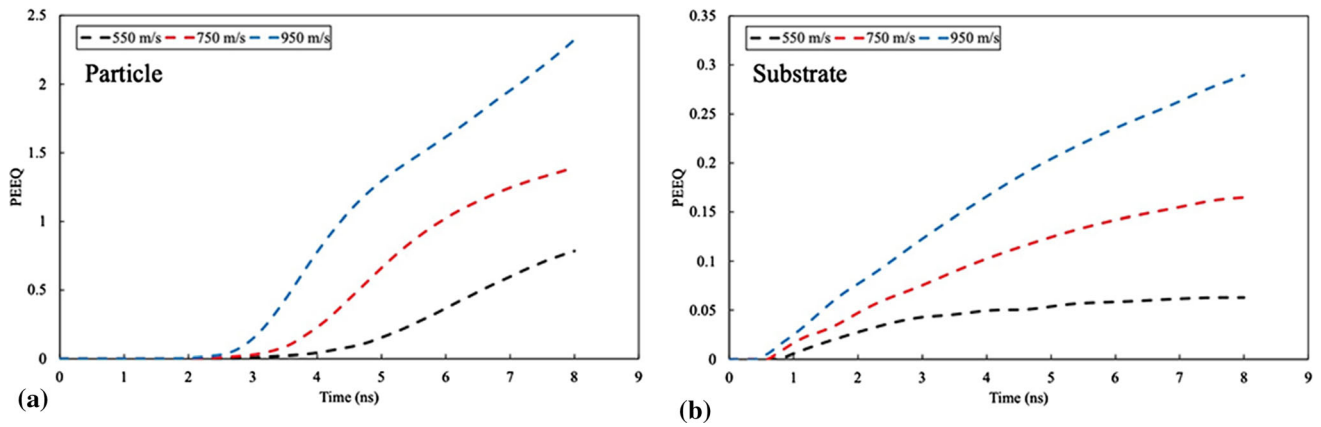


Fig. 10 The effect of impact velocity on the equivalent plastic strain (PEEQ) evolution in the (a) particle and (b) substrate. Initial particle temperature 1073 K and substrate temperature 298 K

Fig. 11 The effect of impact velocity (a) 550 m/s, (b) 750 m/s, and (c) 950 m/s on particle and substrate oxide layer failure, while particle temperature is 1073 K and the substrate temperature is 298 K

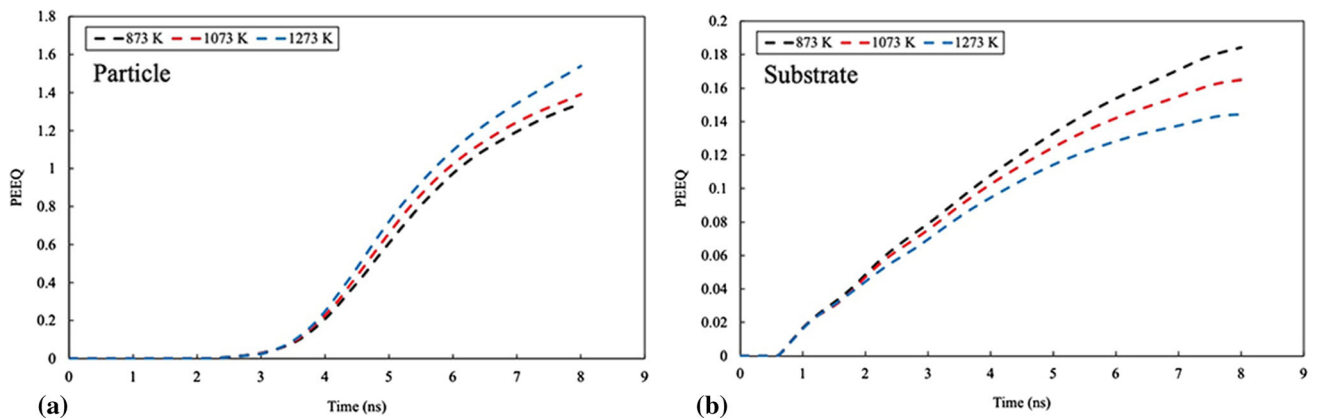
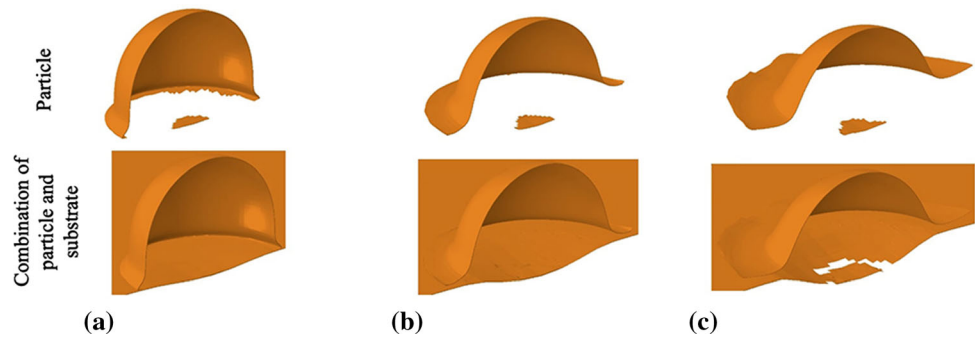


Fig. 12 The effect of particle temperature on the equivalent plastic strain changes by the passage of time for the (a) particle and (b) substrate, while particle velocity is 750 m/s and the substrate temperature is 298 K

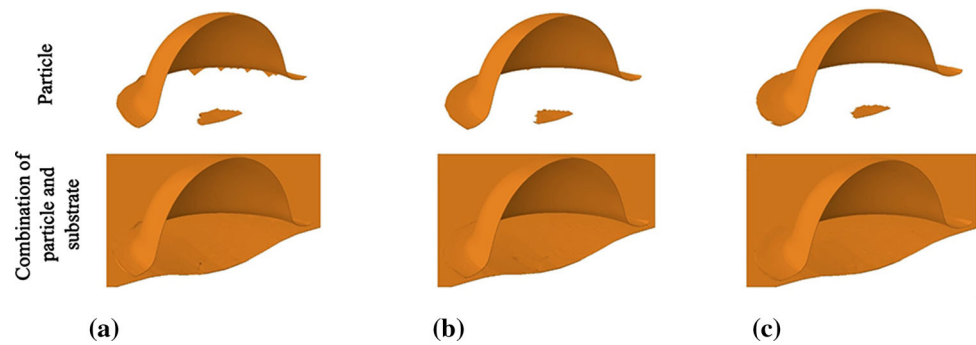
Conclusively, increasing particle velocity can improve the deformation and facilitate substrate oxide layer failure, leading to a stronger adhesion between the particle and the substrate.

Particle Temperature

The influence of particle temperature on the oxide layer failure was studied by assuming that the particle impact on

the substrate surface at the velocity of 750 m/s while particle temperature is 873 K, 1073 K, or 1273 K and the substrate temperature is 298 K. Figure 12 shows the equivalent plastic strain behavior of a particular node of the substrate and the particle. According to Fig. 12(a), particle equivalent plastic strain improved by increasing the particle temperature due to the enhancement of particle thermal softening. Also, Fig. 12(b) illustrates that increasing particle temperature, reduced substrate equivalent plastic

Fig. 13 The effect of particle temperature (a) 873 K, (b) 1073 K, and (c) 1273 K on particle and substrate oxide layer failure, while particle velocity is 750 m/s and the substrate temperature is 298 K



strain and substrate deformation. Hence, it can be concluded that increasing initial particle temperature accelerates the initiation time of particle's oxide layer failure due to an increase in the particle deformation and subsequently the thermal softening effect.

The effect of initial particle temperature on the area where the oxide layer had failed was investigated. As shown in Fig. 13, when particle temperature increases, a larger part of the oxide layer of the particle fails due to the larger degree of particle deformation. This leads to an increase in ASI and the size of the area where two new metallic surfaces were in contact with each other. However, Fig. 13 confirms that at any given particle temperature, the substrate oxide layer remains unaffected and does not fail. This is because the substrate deformation is negatively associated with the particle temperature. Increasing the initial temperature of the particle results in a larger degree of particle deformation; however, it does not lead to a metallurgical bonding because it is ineffective for substrate deformation and substrate oxide layer failure. However, it is worth noting that increasing particle deformation by boosting its temperature can decrease the porosity level of the as-fabricated coating (Ref 23). To our knowledge, the effect of particle temperature on the failure of the oxide layer and adhesive strength between the deposited particle and the substrate has never been experimentally studied. Thus, it is necessary to measure the in-flight particle temperature during the deposition by an inner-diameter HVOF gun for validating the reported simulated outcomes. Also, comparing the results shown in Fig. 11 and 13 suggests that the particle velocity has a greater impact than the particle temperature on the oxide layer failure and the adhesion between particle and substrate (and eventually a metallurgical bonding between the particle and the substrate).

Substrate Temperature

The effect of substrate temperature on oxide layer behavior was investigated by assuming that the particle impact on the substrate surface at the particle velocity of 750 m/s and temperature of 1073 K while the substrate temperature

varied between 298 and 473 K. Figure 14 shows the equivalent plastic strain behavior of the particle and the substrate. According to Fig. 14(a), as substrate temperature increases from 298 to 473 K, the deposited particle plastic strain and deformation have not changed significantly. This is because the heat exchange system between the substrate and particle is adiabatic meaning that no heat would exchange from the substrate to the particle to enhance the particle thermal softening effect in the examined 8 ns. However, the substrate temperature effect on particle deformation has been examined in our previous work for the duration that the particle deformation is completed. It was shown that increasing the substrate temperature can decrease particle flattening ratio and deformation (Ref 23). By increasing substrate temperature, the substrate undergoes a thermal softening effect leading to a rise in equivalent plastic strain. This means that by keeping particle velocity and input kinetic energy constant and increasing substrate temperature, substrate deformation increases, Fig. 14(b).

Finally, the influence of substrate temperature on oxide layer failure is simulated. Figure 15 shows that increasing substrate temperature does not affect the particle oxide layer failure. However, when the substrate temperature is 373 or 473 K, due to the thermal softening effect, the substrate goes through a higher degree of deformation leading to the failure of its oxide layer. Increasing the initial substrate temperature results in the failure of a larger area of its surface. This means that a higher substrate temperature enhances substrate deformation, but its effect on particle deformation is negligible. However, a higher substrate temperature can result in producing an area for metallurgical bonding which was not possible when only the particle temperature was increased (Fig. 13).

Particle and substrate deformation can be altered by increasing substrate temperature and substrate thermal softening effect. This means that by increasing the substrate temperature, the softened substrate would deform more while impacted particles are found to be less deformed (Ref 23). However, pre-heating the substrate can increase substrate oxide layer thickness. The enhanced

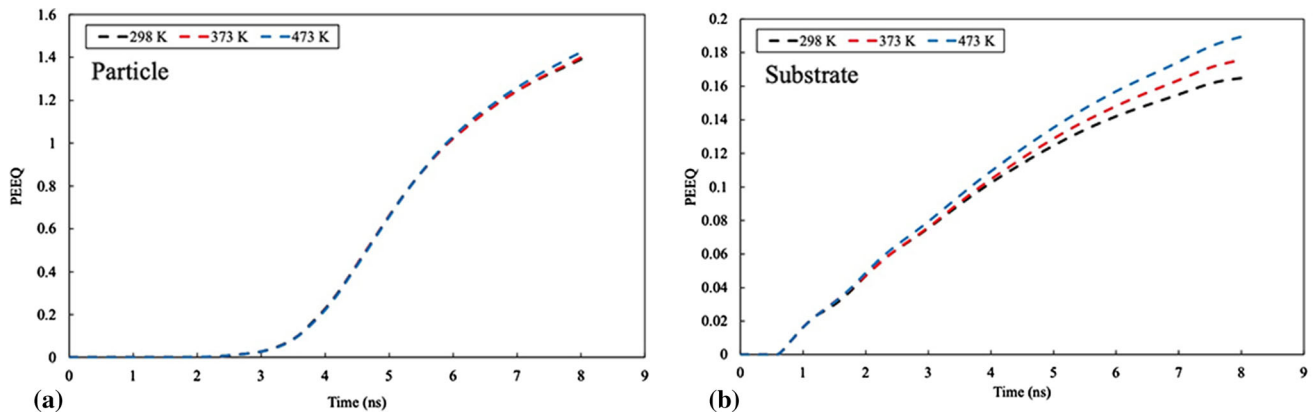
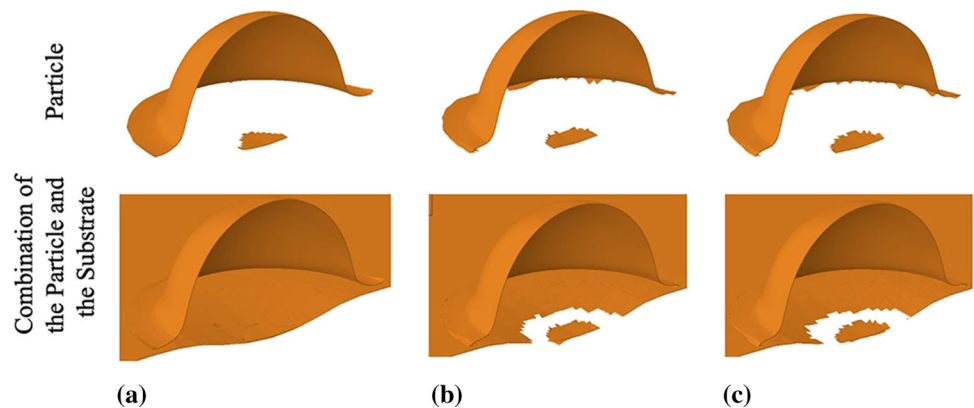


Fig. 14 The effect of substrate temperature on the equivalent plastic strain changes by the passage of time for the (a) particle and (b) substrate, while particle velocity is 750 m/s and particle temperature is 1073 K

Fig. 15 The effect of substrate temperature (a) 298 K, (b) 373 K, and (c) 473 K on particle and substrate oxide layer failure, while particle velocity is 750 m/s and particle temperature is 1073 K



deformation of the pre-heated substrate provides the opportunity to eliminate the substrate thick oxide layer and produce a higher adhesive strength between the particle and substrate (Ref 16).

Conclusion

In this study, a numerical method has been used to investigate the particle and substrate initial conditions on their 80-nm oxide layer failure upon the impact of a deposited Ti-6Al-4V particle using HVAF. Due to the higher gas flow temperature in the HVAF process compared to cold spray, the oxide layer at the surface of the particle and substrate might be thicker, affecting the particle critical velocity. By assuming the existence of an 80-nm oxide layer, it was shown that increasing the particle velocity and substrate temperature can increase the failure of the substrate's oxide layer and, consequently, the adhesion of the particle to the substrate. On the other hand, increasing the particle temperature only affects the particle deformation and has no significant influence on the failure of the substrate oxide layer and the adhesion. However, increasing particle temperature can reduce the porosity level of as-deposited coating. Increasing

substrate temperature can enhance the size of the region in which the oxide layer is broken and the possibility of producing metallurgical bonding exists. Conclusively, this paper illustrated that regardless of material selection, for adhering the particle to the substrate, substrate oxide layer should be broken which is only depended on substrate temperature and impact velocity.

References

1. C. Chen, Y. Xie, X. Yan, S. Yin, H. Fukunuma, R. Huang, R. Zhao, J. Wang, Z. Ren, M. Liu and H. Liao, Effect of Hot Isostatic Pressing (HIP) on Microstructure and Mechanical Properties of Ti6Al4V Alloy Fabricated by Cold Spray Additive Manufacturing, *Addit. Manuf.*, 2019, **27**, p 595-605.
2. S. Bagherifard, S. Monti, M.V. Zucconi, M. Riccio, J. Kondas and M. Guagliano, Cold Spray Deposition for Additive Manufacturing of Freeform Structural Components Compared to Selective Laser Melting, *Mater. Sci. Eng. A*, 2018, **721**, p 339-350.
3. X. Yan, C. Huang, C. Chen, R. Bolot, L. Dembinski, R. Huang, W. Ma, H. Liao and M. Liu, Additive Manufacturing of WC Reinforced Maraging Steel 300 Composites by Cold Spray and Selective Laser Melting, *Surf. Coat. Technol.*, 2019, **371**, p 161-171.
4. P.L. Fauchais, J.V.R. Heberlein and M.I. Boulos, *Thermal Spray Fundamentals from Powders to Parts*, Springer, Cham, 2015.

5. S. Rahmati and A. Ghaei, The Use of Particle/Substrate Material Models in Simulation of Cold-Gas Dynamic-Spray Process, *J. Therm. Spray Technol.*, 2014, **23**, p 530-540.
6. S. Rahmati, R.G.A. Veiga, A. Zuniga and B. Jodoin, A Numerical Approach to Study the Oxide Layer Effect on Adhesion in Cold Spray, *J. Therm. Spray Technol.*, 2021, **30**, p 1777-1791.
7. S. Rahmati and B. Jodoin, Physically Based Finite Element Modeling Method to Predict Metallic Bonding in Cold Spray, *J. Therm. Spray Technol.*, 2020, **29**, p 611-629.
8. Y. Xie, S. Yin, C. Chen, M. Planche, H. Liao and R. Lupoi, New Insights into the Coating/Substrate Interfacial Bonding Mechanism in Cold Spray, *Scripta Mater.*, 2016, **125**, p 1-4.
9. F. Khodabakhshi, B. Marzbanrad, H. Jahed and A.P. Gerlich, Interfacial Bonding Mechanisms between Aluminum and Titanium during Cold Gas Spraying Followed by Friction-Stir Modification, *Appl. Surf. Sci.*, 2018, **462**, p 739-752.
10. T. Schmidt, F. Gartner, H. Assadi and H. Kreye, Development of a Generalized Parameter Window for Cold Spray Deposition, *Acta Mater.*, 2006, **54**, p 729-742.
11. M. Hassani-Gangaraj, D. Veysset, V.K. Champagne, K.A. Nelson and C.A. Schuh, Adiabatic Shear Instability is not Necessary for Adhesion in Cold Spray, *Acta Mater.*, 2018, **158**, p 430-439.
12. C. Chen, Y. Xie, R. Haung, S. Deng, Z. Ren and H. Liao, On the Role of Oxide Film's Cleaning Effects into the Metallurgical Bonding During Cold Spray, *Mater. Lett.*, 2018, **210**, p 199-202.
13. S. Yin, X. Suo, Y. Xie, W. Li, R. Lupoi and H. Liao, Effect of Substrate Temperature on Interfacial Bonding for Cold Spray of Ni onto Cu, *J. Mater. Sci.*, 2015, **50**, p 7448-7457.
14. J.G. Legoux, E. Irissou and C. Moreau, Effect of Substrate Temperature on the Formation Mechanism of Cold-Sprayed Aluminum, Zinc and Tin Coatings, *J. Therm. Spray Technol.*, 2007, **16**, p 616-626.
15. D. Goldbaum, J.M. Shockley, R.R. Chromik, A. Rezaeian, S. Yue, J. Legoux and E. Irissou, The Effect of Deposition Conditions on Adhesion Strength of Ti and Ti6Al4V Cold Spray Splats, *J. Therm. Spray Technol.*, 2012, **21**, p 288-303.
16. Y. Xie, M. Planche, R. Raoulison, H. Liao, X. Suo and P. Herve, Effect of Substrate Preheating on Adhesive Strength of SS 316L Cold Spray Coatings, *J. Therm. Spray Technol.*, 2016, **25**, p 123-130.
17. M. Hassani-Gangaraj, D. Veysset, K.A. Nelson and C.A. Schuh, Impact-Bonding with Aluminum, Silver, and Gold Microparticles: Toward Understanding the Role of Native Oxide Layer, *Appl. Surf. Sci.*, 2019, **576**, p 528-532.
18. Y. Watanabe, C. Yoshida, K. Atsumi, M. Yamada and M. Fukumoto, Influence of Substrate Temperature on Adhesion Strength of Cold-Sprayed Coatings, *J. Therm. Spray Technol.*, 2015, **24**, p 86-91.
19. J. Xie, D. Nelias, H. W. Berre, K. Ogawa, Y. Ichikawa, Simulation of the Cold Spray Particle Deposition Process. *J. Tribol.*, (2015), **137**
20. W.-Y. Li and W. Gao, Some Aspects on 3D Numerical Modeling of High Velocity Impact of Particles in Cold Spraying by Explicit Finite Element Analysis, *Appl. Surf. Sci.*, 2009, **255**, p 7878-7892.
21. H. Assadi, F. Gartner, T. Stoltenhoff and H. Kreye, Bonding Mechanism in Cold Gas Spraying, *Acta Mater.*, 2003, **51**, p 4379-4394.
22. M. Yu, W.-Y. Li, F.F. Wang, X.K. Suo and H.L. Liao, Effect of Particle and Substrate Preheating on Particle Deformation Behavior on Cold Spraying, *Surf. Coat. Technol.*, 2013, **220**, p 174-178.
23. P. Khamsepour, C. Moreau, A. Dolatabadi, Numerical Simulation of the Effect of Particle and Substrate Pre-Heating on Porosity Level and Residual Stress of As-Sprayed Ti6Al4V Components. *J. Therm. Spray Technol.* (2021)
24. W. Li, H. Liao, C. Li, H. Bang and C. Coddet, Numerical Simulation of Deformation Behavior of Al Particles Impacting on Al Substrate and Effect of Substrate Oxide Films on Interfacial Bonding in Cold Spraying, *Appl. Surf. Sci.*, 2007, **253**, p 5084-5091.
25. K. Kim, W. Li and X. Guo, Detection of Oxygen at the Interface and Its Effect on Strain, Stress, and Temperature at the Interface between Cold Sprayed Aluminum and Steel Substrate, *Appl. Surf. Sci.*, 2015, **357**, p 1720-1726.
26. C.M. Almeida, R. Prioli and F.A. Ponce, Effect of Native Oxide Mechanical Deformation on InP Nanoindentation, *J. Appl. Phys.*, 2008, **104**, 113509.
27. O. Heuzé, General Form of the Mie-Grünseisen Equation of State, *C.R. Mec.*, 2012, **340**, p 679-687.
28. Dassault Systemes, 2011, ABAQUS Analysis User's Manuel, 6.11 ed., Simulia
29. X. Wang and J. Shi, Validation of Johnson-Cook Plasticity and Damage Model Using Impact Experiment, *Int. J. Impact Eng.*, 2013, **60**, p 67-75.
30. A. Banerjee, S. Dhar, S. Acharyya, D. Datta and N. Nayak, Determination of Johnson Cook Material and Failure Model Constants and Numerical Modelling of Charpy Impact Test of Armour Steel, *Mater. Sci. Eng. A*, 2015, **640**, p 200-209.
31. Y. Zhang, J.C. Outeiro and T. Mabrouki, On the Selection of Johnson-Cook Constitutive Model Parameters for Ti-6Al-4V Using Three Types of Numerical Models of Orthogonal Cutting, *Proc. CIRP*, 2015, **31**, p 112-117.
32. L.M. Pereira, S. Rahmati, A. Zuniga, B. Jodoin and R.G.A. Veiga, Atomistic Study of Metallurgical Bonding upon the High Velocity Impact of Fcc Core-Shell Particles, *Comput. Mater. Sci.*, 2021, **186**, 110045.
33. K. Nishimura, R.K. Kalia, A. Nakano and P. Vashishta, Nanoindentation Hardness Anisotropy of Alumina Crystal: A Molecular Dynamics Study, *Appl. Phys. Lett.*, 2008, **92**, 161904.
34. C. Zhang, R.K. Kalia, A. Nakano, P. Vashishta and P.S. Branicio, Deformation Mechanisms and Damage in α -Alumina Under Hypervelocity Impact Loading, *J. Appl. Phys.*, 2008, **103**, 083508.
35. A.R. Khoei and M.S. Khorrami, Mechanical Properties of Graphene Oxide: A Molecular Dynamics Study, *Fuller. Nanotub. Carbon Nanostruct.*, 2016, **24**, p 594-603.
36. M.B. Cai, X.P. Li and M. Rahman, Study of the Temperature and Stress in Nanoscale Ductile Mode Cutting of Silicon Using Molecular Dynamics Simulation, *J. Mater. Process. Technol.*, 2007, **192**, p 607-612.
37. C.M. Almeida, R. Prioli and F.A. Ponce, Effect of Native Oxide Mechanical Deformation on InP Nanoindentation, *J. Appl. Phys.*, 2008, **104**, 113509.
38. S.F. Bubar and D.A. Vermilyea, Deformation of Anodic Oxide Films, *J. Electrochem. Soc.*, 1966, **113**, p 892.
39. M. Propp and L. Young, Adhesion, Ductility, and Fracture of Anodic Oxide Films on Tantalum, *J. Electrochem. Soc.*, 1979, **126**, p 624.
40. A. Banerjee, S. Dhar, S. Acharyya, D. Datta and N. Nayak, Determination of Johnson Cook Material and Failure Model Constants and Numerical Modelling of Charpy Impact Test of Armour Steel, *Mater. Sci. Eng. A*, 2015, **640**, p 200-209.
41. J.M. Schreiber, I. Smid, T.J. Eden, K. Koudela, D. Cote and V. Champagne, Cold Spray Particle Impact Simulation Using the Preston-Tonks-Wallace Plasticity Model, *Finite Elem. Anal. Des.*, 2021, **191**, 103557.
42. X. Yan, Q. Li, S. Yin, Z. Chen, R. Jenkins, C. Chen, J. Wang, W. Ma, R. Bolot, R. Lupoi, Z. Ren, H. Liao and M. Liu, Mechanical and In vitro Study of an Isotropic Ti6Al4V Lattice Structure Fabricated Using Selective Laser Melting, *J. Alloy. Compd.*, 2019, **782**, p 209-223.

43. Y. Yang, Temperature-Dependent Thermoelastic Analysis of Multi-dimensional Functionally Graded Materials, Ph.D. thesis, University of Pittsburgh, (2015)
44. M. Sbayti, A. Ghiotti, R. Bahloul, H. Belhadjsalah, S. Bruschi, Finite Element Analysis of Hot Single Point Incremental Forming of hip Prostheses, *MATEC Web of Conferences*, 2016, **80**
45. E. Dong, W. Yu, Q. Cai, L. Cheng and J. Shi, High-Temperature Oxidation Kinetics and Behavior of Ti- 6Al-4V Alloy, *Oxid. Met.*, 2017, **88**, p 719-732.
46. H. Guleryuz and H. Cimenoglu, Oxidation of Ti-6Al-4V Alloy, *J. Alloy. Compd.*, 2009, **472**, p 241-246.
47. H. Fukanuma, N. Ohno, B. Sun and R. Huang, In-flight Particle Velocity Measurements with DPV-2000 in Cold Spray, *Surf. Coat. Technol.*, 2006, **25**, p 1935-1941.
48. <https://spraysensors.tecnar.com/research/dpv/>
49. M.R. Rokni, S.R. Nutt, C.A. Widener, V.K. Champagne and R.H. Hrabe, Review of Relationship Between Particle Deformation, Coating Microstructure, and Properties in High-Pressure Cold Spray, *J. Therm. Spray Technol.*, 2017, **26**, p 1308-1355.
50. V.N.V. Munagala, S.I. Imbriglio and R.R. Chromik, The Influence of Powder Properties on the Adhesion Strength and Microstructural Evolution of Cold Sprayed Ti6Al4V Single Splats, *Mater. Lett.*, 2019, **244**, p 58-61.
51. R. Huang, W. Ma and H. Fukanuma, Development of Ultra-Strong Adhesive Strength Coatings Using Cold Spray, *Surf. Coat. Technol.*, 2014, **258**, p 832-841.
52. A.A. Tiamiyu, X. Chen, E.L. Pang, Y. Sun, J. Lienhard, J.M. LeBeau, K.A. Nelson and C.A. Schuh, Oxide Layer Delamination: An Energy Dissipation Mechanism During High-Velocity Microparticle Impacts, *Appl. Surf. Sci.*, 2022, **574**, p 151673.

Publisher's Note Springer Nature remains neutral with regard to jurisdictional claims in published maps and institutional affiliations.

Springer Nature or its licensor (e.g. a society or other partner) holds exclusive rights to this article under a publishing agreement with the author(s) or other rightsholder(s); author self-archiving of the accepted manuscript version of this article is solely governed by the terms of such publishing agreement and applicable law.